Magnetically induced interfacial instabilities in a ferrofluid annulus

Pedro O. S. Livera [1,*] Pedro H. A. Anjos [2,†] and José A. Miranda [1,‡]
[1]*Departamento de Física, Universidade Federal de Pernambuco, Recife, Pernambuco 50670-901 Brazil*
[2]*Department of Applied Mathematics, Illinois Institute of Technology, Chicago, Illinois 60616, USA*

(Received 22 August 2021; accepted 23 November 2021; published 7 December 2021)

We investigate the flow of a viscous ferrofluid annulus surrounded by two nonmagnetic fluids in a Hele-Shaw cell when subjected to an external radial magnetic field. The interfacial pattern formation dynamics of the system is determined by the interplay of magnetic and surface tension forces acting on the inner and outer boundaries of the annulus, favoring the coupling of the disjoint interfaces. Mode-coupling analysis is employed to examine both linear and weakly nonlinear stages of the flow. Linear stability analysis indicates that the trailing and leading annular boundaries are coupled already at the linear regime, revealing that perturbations arising in the outer interface may induce the emergence of deformed structures in the inner boundary. Moreover, second-order weakly nonlinear analysis is utilized to identify key nonlinear morphological features of the ferrofluid annulus. Our theoretical results show that linear, n-fold symmetric annular patterns having rounded edges are replaced by nonlinear polygonal-like shapes, presenting fairly sharp fingers. It is found that, as opposed to the linear patterns, the nonlinear peaky structures reach a stationary state, characterized by a growth saturation process induced by nonlinear effects. Furthermore, the response of the ferrofluid ring to changes in the thickness of the annulus, in the relative strength of magnetic and surface tensions forces, as well as in the magnetic susceptibility of the ferrofluid material, are also discussed.

DOI: 10.1103/PhysRevE.104.065103

I. INTRODUCTION

The development of interfacial instabilities in radial Hele-Shaw cells is a classical fluid mechanical problem which became a prototypical example of moving interface, pattern-forming phenomena [1]. A Hele-Shaw cell is an experimental device consisting of two parallel glass plates separated by a narrow gap filled with a viscous fluid. When a less-viscous fluid is injected into the more viscous one in this spatially confined cell, the fluid-fluid interface expands radially outwards and becomes unstable, forming fingerlike structures [2–5]. These viscous fingering patterns arise due to the Saffman-Taylor instability [6] which is triggered by the viscosity difference between the fluids. Due to its practical and academic importance, Hele-Shaw cell flows and related interfacial instability phenomena are of primary interest to physicists, applied mathematicians, and engineers and have been studied extensively since the late 1950s.

A particularly interesting variant of the conventional radial Hele-Shaw cell problem, which involves two fluids, and a single interface, is that of a fluid annulus [7–13]. Such an annular fluid configuration establishes three distinct fluid regions, separated by two interfaces: an inner or trailing interface and an outer or leading interface. The fluid annulus setup is of special interest because it involves the interplay between two disjoint interfaces, something that potentially can lead to new phenomenology and still unexplored dynamical behaviors not available in the usual radial Hele-Shaw cell case (where two fluids are separated by one interface).

In the annular injection-driven system, depending on the relative viscosity differences among the fluids, a variety of pattern-forming scenarios may arise. In Ref. [7], Cardoso and Woods performed a linear stability analysis, as well as experiments of such fluid annulus problem in radial Hele-Shaw cells. For the situation in which the trailing interface is highly stable while the other is unstable, one noteworthy finding is the possibility of instability suppression by the continuous thinning of the expanding annulus. Another peculiar observation is the occurrence of a topological instability in which the intermediate fluid annulus eventually ruptures, forming a number of small separate drops. These dual-interface processes (instability suppression and drop formation) are not observed in the usual single-interface problem in radial Hele-Shaw flows. Ward and White [8] also performed experiments for a similar fluid annulus system and analyzed a three-layer radial flow in which an intermediate liquid ring is encircled by two gases. Thus, as opposed to Ref. [7], in Ref. [8] the outer (inner) interface is stable (unstable), and the inner gas can break through the outer annular boundary. Their experiments aimed at measuring average annular film thicknesses, gas phase and total areas, and bursting times. In addition, various different types of interfacial pattern morphologies have been disclosed.

Still within the scope of injection-driven problems in fluid annuli in radial Hele-Shaw cells, more recent studies went beyond ordinary linear stability theory and performed weakly nonlinear analysis [9] and fully nonlinear simulations [10] to examine how nonlinear effects impact the dynamic evolution, and morphological aspects of the spreading fluid annulus.

*pedro.livera@ufpe.br
†pamorimanjos@iit.edu
‡jose.mirandant@ufpe.br

Researchers have also devised alternative controlling strategies to try to restrain increased destabilizing behaviors in dual-interface and multilayer annular fluid systems. This has been done by finding an optimal value for the annulus' viscosity to allow the fastest injection rate possible while maintaining a stable flow [11] or by employing proper time-dependent injection rates [12,13].

The stability and time evolution of fluid annular structures have also been examined in rotating Hele-Shaw cells [14–17]. In this context, the cell rotates about an axis perpendicular to its plates, and centrifugal forces act on the fluids. Therefore, the rotating fluid annulus problem involves the simultaneous action of two different types of morphological instabilities: The traditional, viscosity-contrast-mediated Saffman-Taylor instability and a centrifugally induced one, driven by the density difference of the fluids. Depending on the densities and viscosities of the fluids in the different regions of the cell, distinct scenarios of interfacial instabilities can be considered. References [14,15] carried out two different sets of experiments of a rotating spreading annulus: Reference [14] considers the situation in which the annulus evolves in a stable manner, while Ref. [15] focuses on the linear and nonlinear regimes of the fingering instabilities experienced by the trailing and leading interfaces of the annulus. In these rotating annulus studies, special attention has been devoted to the behavior resulting from the coupled motion of the annular interfaces.

The rotating three-layer fluid system examined in Ref. [15] is particularly appealing since it comprises the development of still uncharted unstable behaviors for the expanding fluid annulus. Distinctive interfacial aspects have been identified, specially in the deep nonlinear regime and in the limit of a very thin annulus. Under these conditions, a phenomenon unique to this annular system has been reported: The formation of thin fluid filaments at the tip of the outgrowing fingers, leading to annular interface breakup, followed by the radial emission of liquid droplets. The doubly connected nature of the rotating annular fluid domain (as opposed to the simply connected character of the corresponding rotating fluid blob problem) has also motivated a number of theoretical studies for the development of time-dependent exact solutions for the rotating fluid annulus interface shape (see, for instance, Refs. [16,17]).

Interesting numerical studies [18,19] investigated a variation of the immiscible rotating fluid annulus situation examined in Refs. [14–17]. In Refs. [18,19] researchers considered the case in which the confined rotating fluids were miscible. Miscible fluids present negligible interfacial tension, and consequently diffusion and convection effects play an important role in determining the shape and dynamic evolution of the expanding annulus. The result of such centrifugally driven, miscible interfacial instability of the annulus is the emergence of even more complex pattern forming structures. It is also worthwhile to note that a recent work [20] analyzed the development of injection-driven, miscible viscous fingering of a fluid annulus without rotation (i.e., miscible analog of the immiscible injection-driven studies performed in Refs. [7–13]) through both numerical computations and laboratory experiments, revealing the formation of very convoluted annular morphologies.

It is worth pointing out that the confined fluid annulus problem has also been studied in another nonstandard Hele-Shaw cell configuration, namely in a lifting Hele-Shaw cell [21–23]. For the lifting plate arrangement with two fluids and one interface, theoretical and experimental analyses usually consider an initially circular blob of viscous fluid surrounded by a fluid of negligible viscosity. In this framing, the upper cell plate is moved upwards uniformly, while the lower plate remains at rest, such that the cell gap is a function of time. The uniform lifting forces the fluid-fluid interface to move inward, making the outer less viscous fluid to penetrate into the inner more viscous fluid. As a result of the Saffman-Taylor instability, visually striking fingering patterns are formed.

The equivalent problem of a fluid annulus in a lifting Hele-Shaw cell has been very recently examined in Ref. [24] via experiments and linear stability analysis. Their dual-interface experiments reveal a considerably different scenario from the one observed in the usual lifting case with just one interface: As the upper plate is lifted, the inner interface deforms, and a single finger arises, while the outer interface remains basically stable. As time progresses, this finger grows, bifurcates at its tip, and eventually reaches the outer interface. Meanwhile, the outer interface is only weakly perturbed. Then, the growing bifurcating finger detaches from the inner interface and erupts to the exterior. As time keeps advancing, an even more complex situation is unveiled, in which a second finger emerges at the inner interface, while intense fingering instabilities arise at the outer boundary and start to move inwards. After that, a very convoluted pattern-forming structured is formed as penetrating fingers moving inward puncture the outward-moving second finger, and cavitation bubbles appear. This sequence of events for the lifting of the fluid annulus makes this situation considerably more complicated than the corresponding lifting case in which only a single interface is present [21–23].

From the material presented above, it is apparent that the consideration of the fluid annulus problem in Hele-Shaw cells introduces a quite diverse spectrum of pattern-forming phenomena and dynamical behaviors which were not present in its single interface counterparts. Nevertheless, in spite of the relevance of the investigations previously performed in the fluid annulus system for various Hele-Shaw cell configurations and different driving forces (injection-driven [7–13], centrifugally induced [14–17], and lifting generated [24]), it is curious to observe that only nonmagnetic fluids have been considered. After all, it is well known that the consideration of magnetic fluids (ferrofluids), subjected to externally applied magnetic fields, introduces the role of a magnetic body force whose action enriches the already diverse pattern formation scenario in Hele-Shaw flows.

Ferrofluids are colloidal suspensions of monodomain nanometer-size magnetic particles suspended in a nonmagnetic carrier fluid [25,26]. These magnetic fluids are Newtonian and present a superparamagnetic behavior, being distinguished by their prompt response to external magnetic stimuli. The unique hydrodynamic and magnetic properties of ferrofluids make them remarkable materials to study a variety of interfacial instabilities and pattern formation processes. This is particularly true for those patterns emerging in Hele-Shaw cells, where depending on the symmetry properties of the applied magnetic field, various interfacial morphologies

have been produced (see, for instance, Refs. [27–37]). Interestingly enough, if, on the one hand, existing fluid annulus investigations have not used ferrofluids, then, on the other hand, it is also valid to say that the study of the dynamics and pattern formation of confined, annular ferrofluid structures has been largely underappreciated in the ferrohydrodynamics literature.

This work aims to begin filling this literature gap by considering a ferrofluid annulus confined in a Hele-Shaw cell, surrounded by a nonmagnetic fluid, and subjected to an applied in-plane radial magnetic field. This opens up the possibility of studying still uninvestigated pattern-forming phenomena in such confined annular magnetic fluid system. This is done by taking into account the influence of magnetic and surface tension effects at the inner and outer interfaces of the ferrofluid ring. We employ a perturbative mode-coupling approach, and perform a linear stability analysis as well as a second-order weakly nonlinear analysis of the problem. While the linear analysis permits access to the stability of both leading and trailing boundaries of the ferrofluid annulus, the inclusion of second-order effects is simply essential to allow one to extract important information about the morphology of such magnetic fluid ring in early nonlinear stages of the flow. It should be emphasized that the weakly nonlinear approach and terminology used in this work have also been previously utilized by many other authors in various perturbative studies of interfacial instabilities in the Rayleigh-Taylor, Saffman-Taylor, and crystal growth problems. For a few examples, please see Refs. [38–46].

The outline of the rest of the paper is as follows. Section II introduces the problem setup and the governing equations and presents the derivation of a set of coupled nonlinear differential equations, which describes the time evolution of the inner and outer interfaces of the ferrofluid annulus. The linear stability aspects of the system are examined in Sec. III A. Then, in Sec. III B, we analyze some relevant features of the pattern formation dynamics in the weakly nonlinear regime. We focus on understanding how the magnetic properties of the ferrofluid, the interplay of magnetic field and surface tension forces, and the coupling of trailing and leading interfaces affect the development of the nonlinear pattern-forming annular structures. Finally, Sec. IV summarizes our main results and provides some concluding remarks.

II. PHYSICAL PROBLEM AND GOVERNING EQUATIONS

The flow configuration of the physical problem is illustrated in Fig. 1. An annular layer of ferrofluid (fluid 2) is separated by two nonmagnetic fluids (fluids 1 and 3). Initially, the fluid-fluid interfaces are circular, having unperturbed radii R_1 and R_2. All fluids are immiscible, incompressible, and Newtonian and have viscosities η_1, η_2, and η_3. The surface tension of the inner (outer) interface is represented by σ_{12} (σ_{23}). The fluids are confined in a Hele-Shaw cell of gap thickness b, and the interfacial destabilization is induced by the action of an externally applied radial magnetic field [35–37],

$$\mathbf{H} = H_0 r\, \hat{\mathbf{r}}, \tag{1}$$

produced by a pair of identical Helmholtz coils, whose electric currents are equal and flow in opposite directions. In Eq. (1),

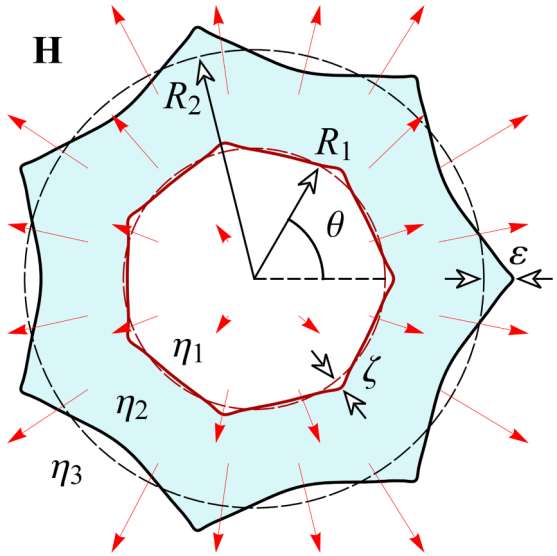

FIG. 1. Schematic of the three-fluid, magnetic field-induced flow in a Hele-Shaw cell. The cell contains an initially circular ferrofluid ringlike structure of radii R_1 and R_2 (dashed circles), and viscosity η_2, surrounded by inner and outer nonmagnetic fluids with viscosities η_1 and η_3. The system is subjected to an in-plane external magnetic field **H** pointing radially outward, which deforms the inner and outer boundaries of the ferrofluid annulus (solid curves). The interfacial perturbation amplitudes in the deformed ferrofluid structure are denoted by $\zeta = \zeta(\theta, t)$ and $\varepsilon = \varepsilon(\theta, t)$, where θ is the azimuthal angle.

H_0 is a constant, r is the radial distance from the origin of the coordinate system (located at the center of the cell), and $\hat{\mathbf{r}}$ is a unit vector in the radial direction. The Hele-Shaw cell is located at the mid-distance between the coils, such that the radial magnetic field is coplanar to it.

Due to the presence of the radial magnetic field, a magnetic body force $\sim M\nabla H$ [25–29,47], where $H = |\mathbf{H}|$ is the local magnetic field intensity, and $M = |\mathbf{M}|$ the magnetization of the ferrofluid, acts on the ferrofluid annulus pulling it along the outward radial direction. In contrast, surface tension forces try to maintain the annular ring shape. As a result of the interplay of these magnetic and capillary forces, the initially circular interfaces of the system can become unstable, and deform. The perturbed shape of the inner interface is expressed as $\mathcal{R}_1 = \mathcal{R}_1(\theta, t) = R_1 + \zeta(\theta, t)$, where θ denotes the azimuthal angle in the r-θ plane (Fig. 1). The net interface disturbance is represented as a Fourier series,

$$\zeta(\theta, t) = \sum_{n=-\infty}^{+\infty} \zeta_n(t)\, e^{\mathrm{i}n\theta}, \tag{2}$$

where $\zeta_n(t)$ denotes the complex Fourier amplitudes, with integer wave numbers n. Likewise, we represent the perturbed shape of the outer interface as $\mathcal{R}_2 = \mathcal{R}_2(\theta, t) = R_2 + \varepsilon(\theta, t)$, where

$$\varepsilon(\theta, t) = \sum_{n=-\infty}^{+\infty} \varepsilon_n(t)\, e^{\mathrm{i}n\theta}. \tag{3}$$

Our perturbative approach keeps terms up to second order in ζ and ε. In both the Fourier expansions of ζ and ε we include the $n = 0$ mode to maintain the area of the intermediate ferrofluid

layer independent of the perturbations. Mass conservation imposes that the zeroth mode is written in terms of the other modes as $\zeta_0 = -(1/2R_1)\sum_{n=1}^{\infty}[|\zeta_n(t)|^2 + |\zeta_{-n}(t)|^2]$ [5]. Similarly, we have $\varepsilon_0 = -(1/2R_2)\sum_{n=1}^{\infty}[|\varepsilon_n(t)|^2 + |\varepsilon_{-n}(t)|^2]$. Since we are interested in the linear and early nonlinear behavior of the annular system, in this section our main task is to derive mode-coupling differential equations which describe the time evolution of the perturbation amplitudes $\zeta_n(t)$ [Eq. (2)] and $\varepsilon_n(t)$ [Eq. (3)], accurate to second order. This will allow us to investigate interesting linear stability issues, as well as to extract valuable information about the important morphological features of the deformed ferrofluid annulus at the onset of nonlinear effects.

By considering the contribution of magnetic forces, the motion of the fluids in the effectively two-dimensional Hele-Shaw cell problem is described by a modified Darcy's law for the gap-averaged velocity [27–29],

$$\mathbf{v}_j = -\frac{b^2}{12\eta_j}\nabla(p_j - \Psi_j), \tag{4}$$

where $p_j = p_j(r,\theta)$ is the pressure and Ψ_j is a scalar potential accounting for the magnetic body force in fluid j ($j = 1, 2, 3$). The subscripts 1, 2, and 3 refer to the inner, intermediate (annulus), and outer fluids, respectively. In Eq. (4), the scalar potential is written as

$$\Psi_j = \frac{\mu_0 \chi H^2}{2}, \tag{5}$$

with μ_0 denoting the magnetic permeability of free space. Consistently with previous studies, in Eq. (5) we assume that the ferrofluid is uniformly magnetized and that the magnetization is collinear with the external magnetic field, $\mathbf{M} = \chi\mathbf{H}$ [25–29,47], where χ is the ferrofluid's constant magnetic susceptibility. It is worth noting that for the nonmagnetic inner and outer fluids $\chi = 0$, and $\Psi_1 = \Psi_3 = 0$. Since the applied magnetic field [Eq. (1)] presents a natural nonzero gradient, we take it as the main local field contribution to the magnetic body force. Under these circumstances, demagnetizing field effects [27–29,47] can be safely neglected.

From Eq. (4), it can be seen that the velocity field is irrotational in the bulk ($\nabla \times \mathbf{v}_j = 0$), and it is convenient to state our moving two-boundary problem in terms of the velocity potentials $\phi_j(r,\theta)$, where $\mathbf{v}_j = -\nabla\phi_j$. In addition, by considering the incompressibility condition $\nabla.\mathbf{v}_j = 0$ one verifies that the velocity potentials obey the Laplace equation $\nabla^2\phi_j = 0$. These velocity potentials can be written as (for $j = 1, 2, 3$)

$$\phi_1(r,\theta) = \sum_{n\neq 0}\alpha(t)\left(\frac{r}{R_1}\right)^{|n|}e^{in\theta}, \tag{6}$$

$$\phi_2(r,\theta) = \sum_{n\neq 0}\beta(t)\left(\frac{r}{R_1}\right)^{-|n|}e^{in\theta} + \sum_{n\neq 0}\gamma(t)\left(\frac{r}{R_2}\right)^{|n|}e^{in\theta}, \tag{7}$$

$$\phi_3(r,\theta) = \sum_{n\neq 0}\omega(t)\left(\frac{r}{R_2}\right)^{-|n|}e^{in\theta}. \tag{8}$$

To find a relationship between the velocity potential coefficients $\alpha(t)$, $\beta(t)$, $\gamma(t)$, and $\omega(t)$ appearing in Eqs. (6)–(8), and the perturbation amplitudes $\zeta_n(t)$ and $\varepsilon_n(t)$ in Eqs. (2) and (3) [and their time derivatives $\dot{\zeta}_n(t)$, and $\dot{\varepsilon}_n(t)$], we use the kinematic boundary condition [1]. This boundary condition expresses the continuity of the normal flow velocity as one crosses each one of the interfaces. In polar coordinates this relation is written for the inner interface as

$$\frac{\partial\mathcal{R}_1}{\partial t} = \left(\frac{1}{r^2}\frac{\partial\mathcal{R}_1}{\partial\theta}\frac{\partial\phi_j}{\partial\theta}\right)\bigg|_{r=\mathcal{R}_1} - \left(\frac{\partial\phi_j}{\partial r}\right)\bigg|_{r=\mathcal{R}_1}, \tag{9}$$

with $j = 1, 2$, and for the outer interface as

$$\frac{\partial\mathcal{R}_2}{\partial t} = \left(\frac{1}{r^2}\frac{\partial\mathcal{R}_2}{\partial\theta}\frac{\partial\phi_j}{\partial\theta}\right)\bigg|_{r=\mathcal{R}_2} - \left(\frac{\partial\phi_j}{\partial r}\right)\bigg|_{r=\mathcal{R}_2}, \tag{10}$$

with $j = 2, 3$.

The second pertinent boundary condition to our dual-interface magnetic problem expresses the pressure jump due to the surface tensions of the interfaces between the successive fluid layers and to the unequal normal magnetic stresses on either side of the ferrofluid annulus. It is given by the augmented Young-Laplace equation [25,26] evaluated at each interface,

$$(p_1 - p_2)|_{r=\mathcal{R}_1} = \left[\sigma_{12}\kappa_{12} + \frac{1}{2}\mu_0(\mathbf{M}\cdot\hat{\mathbf{n}})^2\right]\bigg|_{r=\mathcal{R}_1}, \tag{11}$$

$$(p_2 - p_3)|_{r=\mathcal{R}_2} = \left[\sigma_{23}\kappa_{23} - \frac{1}{2}\mu_0(\mathbf{M}\cdot\hat{\mathbf{n}})^2\right]\bigg|_{r=\mathcal{R}_2}, \tag{12}$$

where

$$\kappa_{12} = \frac{\mathcal{R}_1^2 + 2\left(\frac{\partial\mathcal{R}_1}{\partial\theta}\right)^2 - \mathcal{R}_1\frac{\partial^2\mathcal{R}_1}{\partial\theta^2}}{\left[\mathcal{R}_1^2 + \left(\frac{\partial\mathcal{R}_1}{\partial\theta}\right)^2\right]^{3/2}}$$

and

$$\kappa_{23} = \frac{\mathcal{R}_2^2 + 2\left(\frac{\partial\mathcal{R}_2}{\partial\theta}\right)^2 - \mathcal{R}_2\frac{\partial^2\mathcal{R}_2}{\partial\theta^2}}{\left[\mathcal{R}_2^2 + \left(\frac{\partial\mathcal{R}_2}{\partial\theta}\right)^2\right]^{3/2}}.$$

In Eqs. (11) and (12), κ_{12} and κ_{23} denote the interfacial curvatures of the inner and outer interfaces in the plane of the Hele-Shaw cell, respectively. In addition, $\hat{\mathbf{n}}|_{r=\mathcal{R}_{1,2}}$ represents the unit normal vectors at the interfaces [$\hat{\mathbf{n}}_{r=\mathcal{R}_1} = [\nabla(r - \mathcal{R}_1)/|\nabla(r-\mathcal{R}_1)|]_{r=\mathcal{R}_1}$ and $\hat{\mathbf{n}}_{r=\mathcal{R}_2} = [\nabla(r-\mathcal{R}_2)/|\nabla(r-\mathcal{R}_2)|]_{r=\mathcal{R}_2}$]. The term proportional to $(\mathbf{M}\cdot\hat{\mathbf{n}})^2$ on the right-hand side of Eqs. (11) and (12) is commonly known as the magnetic normal traction term [25,26] and incorporates the influence of the discontinuous normal component of the magnetization at the interfaces.

At this stage of our calculation, we have all elements necessary to find the set of mode-coupling differential equations for the perturbation amplitudes $\zeta_n(t)$ and $\varepsilon_n(t)$. Following usual procedures adopted in previous weakly nonlinear studies (see, for instance, Refs. [5,9,36]) in Hele-Shaw cells, we perform Fourier expansions for the velocity potentials [Eqs. (6)–(8)] and use the kinematic boundary condition [Eqs. (9) and (10)] to express the Fourier coefficients of ϕ_j [i.e., $\alpha(t)$, $\beta(t)$, $\gamma(t)$, and $\omega(t)$] in terms of ζ_n, ε_n, and their time derivatives. Substituting these relations, and the pressure jump condition [Eqs. (11) and (12)] into Darcy's law [Eq. (4)] and keeping

terms up to second order in ζ and ε, we obtain the set of dimensionless coupled equations of motion for both the perturbation amplitudes ζ_n and ε_n (for $n \neq 0$)

$$\begin{aligned}\dot{\zeta}_n = {} & f_1\,\Lambda(n)\zeta_n + f_2\,\Gamma(n)\varepsilon_n \\ & + f_1 \sum_{n'\neq 0}[F(n,n')\zeta_{n'}\zeta_{n-n'} + G(n,n')\dot{\zeta}_{n'}\zeta_{n-n'}] \\ & + f_2 \sum_{n'\neq 0}[H(n,n')\varepsilon_{n'}\varepsilon_{n-n'} + I(n,n')\dot{\varepsilon}_{n'}\varepsilon_{n-n'}] \\ & + f_2 \sum_{n'\neq 0}[J(n,n')\dot{\zeta}_{n'}\varepsilon_{n-n'} + K(n,n')\dot{\varepsilon}_{n'}\zeta_{n-n'}], \end{aligned} \tag{13}$$

and

$$\begin{aligned}\dot{\varepsilon}_n = {} & f_3\,\Lambda(n)\zeta_n + f_4\,\Gamma(n)\varepsilon_n \\ & + f_4 \sum_{n'\neq 0}[\mathcal{F}(n,n')\varepsilon_{n'}\varepsilon_{n-n'} + \mathcal{G}(n,n')\dot{\varepsilon}_{n'}\varepsilon_{n-n'}] \\ & + f_3 \sum_{n'\neq 0}[\mathcal{H}(n,n')\zeta_{n'}\zeta_{n-n'} + \mathcal{I}(n,n')\dot{\zeta}_{n'}\zeta_{n-n'}] \\ & + f_3 \sum_{n'\neq 0}[\mathcal{J}(n,n')\dot{\varepsilon}_{n'}\zeta_{n-n'} + \mathcal{K}(n,n')\dot{\zeta}_{n'}\varepsilon_{n-n'}], \end{aligned} \tag{14}$$

where the overdot represents a total time derivative. In Eqs. (13) and (14) lengths and time are rescaled by $L = r_0$ and $T = 12(\eta_3 + \eta_2)r_0^3/\sigma_{23}b^2$, respectively, where r_0 is a characteristic length being on the order of the unperturbed radii R_1 and R_2. From this point onward, unless otherwise stated, we use a dimensionless version of the equations. In addition,

$$\Lambda(n) = \left[-\mathcal{A}|n|N_B\chi(1+\chi) - \frac{\sigma}{R_1^3}\mathcal{A}|n|(n^2-1)\right] \tag{15}$$

and

$$\Gamma(n) = \left[|n|N_B\chi(1+\chi) - \frac{1}{R_2^3}|n|(n^2-1)\right] \tag{16}$$

are time-independent functions. The somewhat complicated expressions for the nonlinear mode-coupling functions F, G, H, I, J, K, $\mathcal{F}$, $\mathcal{G}$, $\mathcal{H}$, $\mathcal{I}$, $\mathcal{J}$, and $\mathcal{K}$ are given in the Appendix [see Eqs. (A1)–(A16)]. In Eqs. (13) and (14)

$$f_1 = \frac{1 - A_{23}R^{2|n|}}{1 + A_{12}A_{23}R^{2|n|}}, \qquad f_2 = \frac{1 + A_{12}}{1 + A_{12}A_{23}R^{2|n|}}R^{|n|-1},$$
$$f_3 = \frac{1 - A_{23}}{1 + A_{12}A_{23}R^{2|n|}}R^{|n|+1}, \qquad f_4 = \frac{1 + A_{12}R^{2|n|}}{1 + A_{12}A_{23}R^{2|n|}},$$

where $A_{12} = (\eta_2 - \eta_1)/(\eta_2 + \eta_1)$ $[A_{23} = (\eta_3 - \eta_2)/(\eta_3 + \eta_2)]$ is the viscosity contrast of fluids 1 and 2 [2 and 3] and $\mathcal{A} = (\eta_3 + \eta_2)/(\eta_2 + \eta_1)$. The ratio of the unperturbed radii

$$R = \frac{R_1}{R_2} \tag{17}$$

plays an important role in our system as it measures the coupling strength between the interfaces [9–11], and

$$N_B = \frac{\mu_0 H_0^2 r_0^3}{\sigma_{23}} \tag{18}$$

represents the magnetic Bond number, which quantifies the ratio of magnetic to capillary forces. In addition, $\sigma = \sigma_{12}/\sigma_{23}$ is the ratio of the surface tensions.

Equations (13) and (14) represent the mode-coupling expressions describing the shapes of the boundaries of a ferrofluid annulus subjected to an external radial magnetic field in the confined setting of a Hele-Shaw cell. Note that these equations are already coupled at the linear level (first order in ζ_n and ε_n), meaning that any disturbance growing in one of the interfaces may impact the dynamics of the other. As will become clear during the course of this paper, our mode-coupling method offers the possibility to assess key morphological features arising at the ferrofluid interfaces, and their dependence on the most relevant parameters of the system (R, N_B, and χ).

Observe that in the limit of a very thick ferrofluid annulus, the interfaces decouple. This physical situation corresponds to the limit $R \to 0$ such that $(f_1, f_4) \to 1$, and $(f_2, f_3) \to 0$ in Eqs. (13) and (14), yielding

$$\dot{\zeta}_n = \Lambda(n)\,\zeta_n + \sum_{n'\neq 0}[F(n,n')\zeta_{n'}\zeta_{n-n'} + G(n,n')\dot{\zeta}_{n'}\zeta_{n-n'}] \tag{19}$$

and

$$\dot{\varepsilon}_n = \Gamma(n)\,\varepsilon_n + \sum_{n'\neq 0}[\mathcal{F}(n,n')\varepsilon_{n'}\varepsilon_{n-n'} + \mathcal{G}(n,n')\dot{\varepsilon}_{n'}\varepsilon_{n-n'}]. \tag{20}$$

In this scenario, which characterizes the two-fluid single-interface limit, it can be shown that after appropriate reintroduction of dimensions, Eq. (19) describes the interfacial behavior of a nonmagnetic fluid droplet with viscosity η_1 surrounded by a ferrofluid with viscosity η_2, where $\Lambda(n)$ [Eq. (15)] is the time-independent growth rate of the flow. Note that this situation is stable, and the interface tends to maintain its circular shape since $\Lambda(n) < 0$ for all the Fourier modes n, and for any parameter values. Likewise, Eq. (20) represents the interface behavior of a ferrofluid droplet with viscosity η_2 surrounded by a nonmagnetic fluid with viscosity η_3, where $\Gamma(n)$ [Eq. (16)] is the time-independent growth rate. In this case, some of the Fourier modes have a positive growth rate [$\Gamma(n) > 0$] depending on the value of N_B, and the flow can be unstable. Equations (19) and (20) are in agreement with previous expressions obtained in Refs. [35,36] for two-fluid, single-interface, magnetic field-induced flow problems in Hele-Shaw cells. We point out that to reinforce the pragmatic and academic relevance of our theoretical results, throughout this work, we utilize typical parameter values that are consistent with the ones used in existing experimental studies of pattern formation in ferrofluids [29,30,48–55].

III. DISCUSSION

A. Linear dynamics of the coupled interfaces

Considering that the two interfaces of the ferrofluid annulus are already coupled at the linear level, prior to addressing the nonlinear issues connected to the morphology of the pattern-forming structures, we first discuss some noteworthy features of the linear regime. In this section, our leading goal is to analyze the very early time dynamics of the interfaces

as the coupling strength parameter R is varied. In this initial time regime, the two interfaces are just mildly deformed by magnetic forces. Under these conditions, the interfacial perturbations ζ and ε are so small that second-order terms in Eqs. (13) and (14) can be neglected. Within this linear framework, the equations of motion for the perturbation amplitudes [(13) and (14)] are significantly simplified, being reduced to

$$\dot{\zeta}_n = f_1\ \Lambda(n)\zeta_n + f_2\ \Gamma(n)\varepsilon_n \tag{21}$$

and

$$\dot{\varepsilon}_n = f_3\ \Lambda(n)\zeta_n + f_4\ \Gamma(n)\varepsilon_n. \tag{22}$$

Equations (21) and (22) form a system of coupled first-order ordinary differential equations (ODEs), presenting constant (in time) coefficients.

In order to solve the system of ODEs, we first rewrite Eq. (21) as

$$\varepsilon_n = \frac{\dot{\zeta}_n - f_1\ \Lambda(n)\zeta_n}{f_2\ \Gamma(n)}, \tag{23}$$

and substitute it into Eq. (22) to obtain

$$\ddot{\zeta}_n - [f_1\Lambda(n) + f_4\Gamma(n)]\dot{\zeta}_n + [(f_1 f_4 - f_2 f_3)\Lambda(n)\Gamma(n)]\zeta_n = 0. \tag{24}$$

Taking the initial conditions as $\zeta_n(0) = \varepsilon_n(0)$ and $\dot{\zeta}_n(0) = [f_1\ \Lambda(n) + f_2\ \Gamma(n)]\zeta_n(0)$ [obtained from Eq. (23) evaluated at $t = 0$], this second-order ODE can be easily solved, yielding

$$\zeta_n(t) = \frac{\zeta_n(0)}{2\delta(n)}\{[f_1\ \Lambda(n) + (2f_2 - f_4)\ \Gamma(n)]f_-(n,t) + \delta(n)f_+(n,t)\}. \tag{25}$$

Finally, by substituting the previous result back into Eq. (23), we have

$$\varepsilon_n(t) = \frac{\varepsilon_n(0)}{2\delta(n)}\{[(2f_3 - f_1)\ \Lambda(n) + f_4\ \Gamma(n)]f_-(n,t) + \delta(n)f_+(n,t)\}, \tag{26}$$

where

$$\delta(n) = \sqrt{[f_1\ \Lambda(n) - f_4\ \Gamma(n)]^2 + 4f_2 f_3\ \Lambda(n)\Gamma(n)} \tag{27}$$

and

$$f_\pm(n,t) = \exp\left\{\frac{t}{2}[f_1\ \Lambda(n) + f_4\ \Gamma(n) + \delta(n)]\right\} \pm \exp\left\{\frac{t}{2}[f_1\ \Lambda(n) + f_4\ \Gamma(n) - \delta(n)]\right\}. \tag{28}$$

Equations (25) and (26) describe the linear time evolution of the perturbations growing (or decaying) in the inner and outer interfaces, respectively. From these relations one obtains the linear growth rates of the ferrofluid annular system

$$\lambda_1(n,t) \equiv \frac{\dot{\zeta}_n}{\zeta_n} = f_1\ \Lambda(n) + f_2\ \Gamma(n)\frac{\varepsilon_n(t)}{\zeta_n(t)} \tag{29}$$

and

$$\lambda_2(n,t) \equiv \frac{\dot{\varepsilon}_n}{\varepsilon_n} = f_3\ \Lambda(n)\frac{\zeta_n(t)}{\varepsilon_n(t)} + f_4\ \Gamma(n). \tag{30}$$

Note that both growth rates [Eqs. (29) and (30)] do depend on time, in contrast to the time-independent growth rates [Eqs. (15) and (16)] found in the simpler two-fluid, magnetic field-induced flow which has a single interface. Another unique feature of three-fluid, ferrofluid annulus problem is the fact that even if one of the interfaces is initially (at $t = 0$) stable, i.e., $\lambda_1(n, t = 0) < 0$ or $\lambda_2(n, t = 0) < 0$, it may become unstable for subsequent times (for $t > 0$) due to the influence of the other interface. Therefore, already at the linear level, the ferrofluid annulus system presents a richer dynamics than its two-fluid, single interface counterpart [35,36].

To investigate the effects of the coupling strength parameter R at the linear level of the annular ring dynamics, in Fig. 2 we plot the two linear growth rates $\lambda_1(n,t)$ [Eq. (29)] and $\lambda_2(n,t)$ [Eq. (30)] of the system as functions of mode n, at time values $t = 0$ [Figs. 2(a) and 2(d)], $t = 10^{-3}$ [Figs. 2(b) and 2(e)], and $t = 2.2 \times 10^{-3}$ [Figs. 2(c) and 2(f)]. This is done for $R = 0.3$, depicted in the top row panels, and $R = 0.9$, shown in the bottom row panels. Recall that R [Eq. (17)] is simply the ratio of the unperturbed radii of the ferrofluid annulus, and since we take $R_2 = 1$ and $R_1 = R$, this dimensionless parameter is related to the initial ferrofluid ring thickness through the relation $1 - R$. Therefore, larger values of R are associated with thinner annuli. Moreover, with no loss of generality, we consider the characteristic physical parameters $N_B = 136$, $\chi = 0.8$, $A_{12} = \mathcal{A} = 1$, $A_{23} = -1$, $R_2 = 1$, $R_1 = R$, and $\sigma = 1$.

First, we analyze the case in which $R = 0.3$, meaning that the coupling between the interfaces is not so strong. By inspecting Fig. 2(a), we verify that the growth rate $\lambda_2(n,t)$ of the outer interface is positive in the interval $2 \leqslant n \leqslant 14$ and reaches its largest value at approximately $n = 8$. These findings provide useful information about the band of unstable modes and the wave number of maximum growth (or the dominant mode), respectively. As time progresses, neither of these features are significantly affected, as one can observe in the graphs illustrated in Figs. 2(b) and 2(c). However, note that while $\lambda_2(n,t)$ almost does not change with time, $\lambda_1(n,t)$ is remarkably altered by it. At time $t = 0$, we observe that $\lambda_1(n,t)$ is negative for any mode n [Fig. 2(a)], meaning that the inner interface is linearly stable against perturbations of any wave number. With the increase of time, this curve starts to become positive, first for higher modes n [Fig. 2(b)] and later for all the modes inside the band of unstable modes of $\lambda_2(n,t)$ [Fig. 2(c)]. Note that at $t = 2.2 \times 10^{-3}$, the two curves are very similar to each other, and for larger values of time (not presented here), they overlap and stop to vary with time. We emphasize that this does not mean that the system reaches a stationary state but rather that, from this point onward, the linear disturbances in both interfaces grow at a constant rate.

Now we turn our attention to the bottom row of Fig. 2, where the value $R = 0.9$ is considered, and therefore the coupling strength is stronger than the situation analyzed in Figs. 2(a)–2(c). We can see that difference in the dynamics of the system begins already at $t = 0$: In Fig. 2(d), both growth rates have small positive values for some modes n; however, the band of unstable modes, the dominant mode, and also the magnitude of $\lambda_2(n,t)$ are significantly reduced when compared to the equivalent situation presented in Fig. 2(a) for $R = 0.3$. When the interfacial coupling is more intense, one can see that both growth rates evolve in time as two very similar curves [Fig. 2(e)], and, finally, in Fig. 2(f), we observe

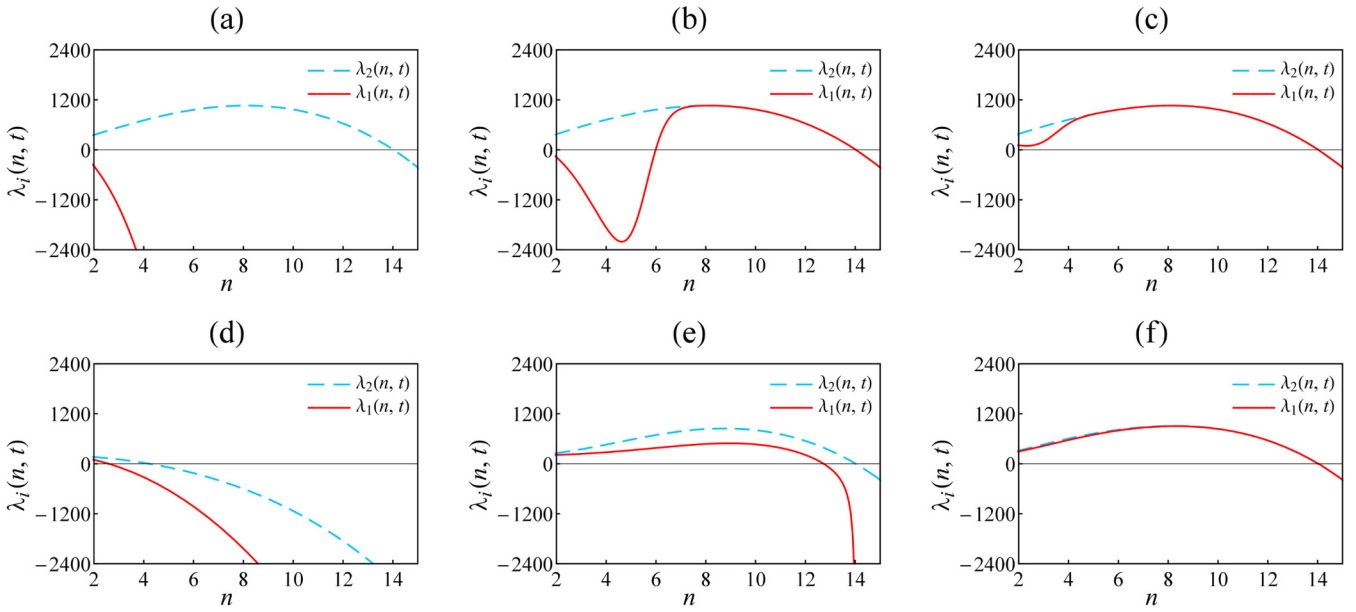

FIG. 2. Linear growth rates $\lambda_i(n,t)$ with $i=1,2$, as a function of the azimuthal wave number n for $R=0.3$ (top panels) and $R=0.9$ (bottom panels), and three values of time: $t=0$ [(a) and (d)], $t=10^{-3}$ [(b) and (e)], and $t=2.2\times10^{-3}$ [(c) and (f)]. In addition, we set $N_B=136$, $\chi=0.8$, $A_{12}=\mathcal{A}=1$, $A_{23}=-1$, and $\sigma=1$.

that the curves are almost indistinguishable. Therefore, for situations in which R is large, we expect that the interfaces evolve linearly to almost the same final shape, aside from a small difference in the perturbation magnitudes. The findings unveiled by Fig. 2 highlight the importance of the coupling strength parameter R in the dynamics of our three-fluid, magnetic field-induced flow.

Although the analysis of the linear growth rates performed in Fig. 2 is a useful way to gain insights into the early time evolution of the system, these linear predictions are better visualized by examining the pattern-forming structures that emerge for the inner and outer interfaces of the ferrofluid annulus. Therefore, in Fig. 3 we present the linear time evolution of the ferrofluid annulus for three increasing values of coupling strength parameter: $R=0.75$ for the top panels [Figs. 3(a)–3(c)], $R=0.92$ for the middle panels [Figs. 3(d)–3(f)], and $R=0.95$ for the bottom panels [Figs. 3(g)–3(i)]. The linear interfaces are obtained by using Eqs. (25) and (26). We consider the interplay of a finite number N of Fourier modes and rewrite Eqs. (2) and (3) in terms of the real-valued cosine amplitudes $a_n(t)=\zeta_n(t)+\zeta_{-n}(t)$ [$\bar{a}_n(t)=\varepsilon_n(t)+\varepsilon_{-n}(t)$]. More specifically, most of the patterns in this work are generated considering $N=80$ Fourier modes, namely the fundamental mode $n=8$ and its harmonics $2n$, $3n,\ldots,$ and $80n$. This large number of participating modes ($N=80$) is justified in order to guarantee that the edges of the fingering patterns are quite smooth. This is especially true for the nonlinear patterns that will be shown in Sec. III B. Without loss of generality, we choose the phase of the fundamental mode so that $a_n>0$, $\bar{a}_n>0$. In addition, we take the initial conditions $a_n(0)=\bar{a}_n(0)=a_{2n}(0)=\bar{a}_{2n}(0)=\ldots=a_{80n}(0)=\bar{a}_{80n}(0)=10^{-5}$. We point out that the numerical calculations leading to the various patterns shown in this work have been performed by using the software package Mathematica.

Throughout this work, we assume that the fundamental mode is given by the closest integer to the fastest growing mode at the final time t_f of the evolution (i.e., the mode of maximum growth rate $n_{\max}$). Note that $n_{\max}$ is obtained by evaluating either $[d\lambda_1(n,t=t_f)/dn]|_{n=n_{\max}}$ or $[d\lambda_2(n,t=t_f)/dn]|_{n=n_{\max}}$, since both growth rates overlap very rapidly for times smaller than the final times t_f considered in Fig. 3. Each row of Fig. 3 corresponds to a different time evolution, and the patterns are depicted at the times (a) $t=7.0\times10^{-3}$, (b) $t=8.0\times10^{-3}$, (c) $t=8.6\times10^{-3}$, (d) $t=9.5\times10^{-3}$, (e) $t=1.1\times10^{-2}$, (f) $t=1.15\times10^{-2}$, (g) $t=1.2\times10^{-2}$, (h) $t=1.4\times10^{-2}$, and (i) $t=1.52\times10^{-2}$. Note that the values of t_f used in Fig. 3(c), Fig. 3(f), and Fig. 3(i) are not arbitrary. They are defined as the times at which the amplitude of the fundamental mode of the outer interface has reached the same magnitude [namely $\bar{a}_n(t=t_f)\approx7.7\times10^{-2}$] for each value assumed by R. Recall that the perturbations that emerge in the outer interface may trigger instabilities in the inner interface depending on the value of R. Therefore, by keeping $\bar{a}_n(t=t_f)$ fixed in each one of these three time evolutions, we guarantee that the influence of the outer interface over the inner boundary is equal, and in that way, any changes in the shape of the inner interface are solely due to the interplay of magnetic and surface tension effects in the ferrofluid annulus. Finally, we point out that all the other physical parameters are the same as those utilized in Fig. 2.

Before we begin the morphological analysis of the patterns displayed in Fig. 3, we would like to stress that although these patterns are plotted for almost the same set of physical parameters utilized to plot Fig. 2, in Fig. 3, we have modified some of the parameters. More specifically, in Fig. 3, we utilize $R=0.75$, $R=0.92$, and $R=0.95$, in contrast to the values $R=0.3$, and $R=0.9$ employed in Fig. 2. Moreover, the values of final times used in Fig. 3 are also larger than the values utilized in Fig. 2. Therefore, one should not interpret

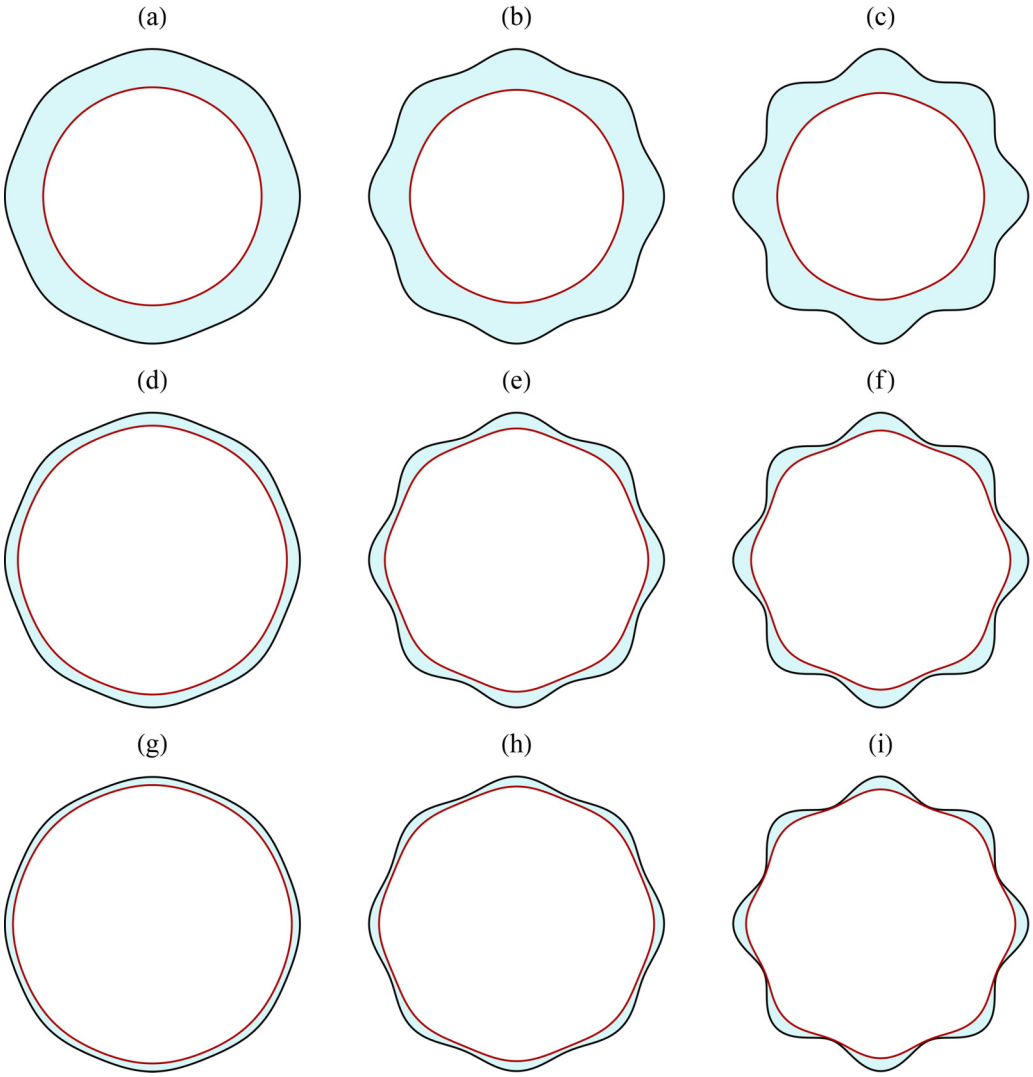

FIG. 3. Snapshots illustrating the typical purely linear evolution of the ferrofluid annulus patterns for $R = 0.75$ (top panels), $R = 0.92$ (middle panels), and $R = 0.95$ (bottom panels). Each row corresponds to a different time evolution, and the values of time t utilized are the following: (a) $t = 7.0 \times 10^{-3}$, (b) $t = 8.0 \times 10^{-3}$, (c) $t = 8.6 \times 10^{-3}$, (d) $t = 9.5 \times 10^{-3}$, (e) $t = 1.1 \times 10^{-2}$, (f) $t = 1.15 \times 10^{-2}$, (g) $t = 1.2 \times 10^{-2}$, (h) $t = 1.4 \times 10^{-2}$, and (i) $t = 1.52 \times 10^{-2}$. Moreover, these patterns are generated by considering $N = 80$ $(n, 2n, 3n, \ldots, 80n)$ participating cosine modes, where $n = 8$ is the fundamental mode. All the other physical parameters are identical to those utilized in Fig. 2.

the patterns depicted in Fig. 3 as the fingered structures corresponding to the situations presented in Fig. 2. It should be clear that these modifications were employed just as a way to better illustrate, in a more visual fashion, the impact of R on the morphology of the linear interfaces.

We initiate our discussion by examining the pattern-forming dynamics shown in the first row of Fig. 3 [Figs. 3(a)–3(c)] for $R = 0.75$. In Fig. 3(a), we can observe a thick ferrofluid annulus delimited by a mildly deformed outer interface and an almost circular inner interface. As time advances, the inner interface keeps its circular shape, but eight small, smooth protrusions start to take form in the outer interface, as one can see in Fig. 3(b). This eightfold sinusoidal shape is determined by the growth of the fundamental mode $n = 8$, which reaches much larger amplitudes than its harmonic modes $(2n, 3n, \ldots,$ and $80n)$. When time advances even further, the perturbation amplitude of the fundamental mode $\bar{a}_n$ continues to increase, and one observes that the fingers of the outer interface grow larger in length. Conversely, the inner interface exhibits just a very modest onset of perturbation growth. Therefore, for the values $t = 8.6 \times 10^{-3}$ and $R = 0.75$ considered in Fig. 3(c), the coupling between the interfaces is relatively weak, and the inner boundary does not change much with respect to its initial circular shape.

In Figs. 3(d)–3(f) we present the time evolution of the ferrofluid annulus for $R = 0.92$, a case in which the coupling between the interfaces is stronger than the situation in Figs. 3(a)–3(c) for $R = 0.75$. By comparing the initial pattern depicted in Fig. 3(d) with the structure found in Fig. 3(a), we can only point to the fact that the ferrofluid annulus in Fig. 3(d) is thinner but that the interfaces look very similar to those shown in Fig. 3(a). Nevertheless, the difference between the dynamics of the first and second rows of Fig. 3 starts to become more evident as time increases. In Fig. 3(e), in contrast to what was found in Fig. 3(b), we verify that both the outer as well as the inner interfaces present fingered perturbations.

This behavior becomes even more apparent in Fig. 3(f), in which both boundaries exhibit a legitimate eightfold shape, with the outer interface being more unstable than the inner one. We stress that, although the final times t_f in the cases depicted in Fig. 3(c) and Fig. 3(f) are different, the amplitudes of the fundamental mode of the outer interface $[\bar{a}_n(t_f)]$ are equal. In this way, the more prominent eightfold shape exhibited by the inner interface in Fig. 3(f) is due to the augmented influence of the outer interface over the inner interface provided by the thinner ferrofluid annulus. As a matter of fact, this effect is even more clear when we utilize a larger value of R, as shown in the bottom row of Fig. 3 for $R = 0.95$ [Figs. 3(g)–3(i)]. In particular, the inner interface found in Fig. 3(i) is not only more unstable than the inner boundaries shown in Figs. 3(c) and 3(f) but also acquires a similar shape to the outer interface, as if the two interfaces had evolved almost as a single one. One very important point to be stressed is the fact that the final time shapes illustrated in Figs. 3(c), 3(f), and 3(i) are *not* stationary states. We have verified that, at the linear level, the perturbation mode amplitudes grow very rapidly as time progresses and do not reach a stationary value. Consequently, if one goes beyond $t = t_f$, then the length of the fingers increase exponentially. As a result, the trailing and leading interfaces cross one another, and our perturbative approach is no longer valid.

The physical reason behind the time dependence in the linear growth rates discussed in Figs. 2 and 3 emerges due to fluid-dynamic and magnetic interactions between the inner and outer interfaces of the annular structure, whose intensity is related to the thickness of the ferrofluid annulus. However, the fact that the interfaces are physically connected in this fashion does not necessarily imply a time dependence in the linear growth rates. Therefore, a key point to understand this phenomenon at the linear level is to note that what triggers growth of instabilities on the inner interface is the emergence of disturbances in the always linearly unstable outer interface [see Eq. (16)]. So the time-dependent disturbances $[\varepsilon_n(t)]$ arising in the outer interface are transferred, via finite-size effects of the annulus, to the inner boundary, influencing its linear stability, and thus making its growth rate dependent on $\varepsilon_n(t)$ or, equivalently, on time. Note that if, for some reason, perturbations on the outer interface are absent, i.e., if $\varepsilon_n(t) = 0$, then the outer interface would not impact the inner interfaces stability regardless of the annulus thickness (value of R), and, in that case, its linear growth rate would be independent of time. This physical interpretation is contained in Eqs. (15), (16), (29), and (30).

The linear results extracted from Figs. 2 and 3 complement each other and thoroughly illustrate the characteristic linear dynamic behavior of the disjoint interfaces of the ferrofluid annulus, under the influence of an applied radial magnetic field. Nevertheless, it is a well-known fact that, although purely linear theory provides useful answers concerning the system's stability issues, it usually fails to capture the inner and outer interfaces' morphologies accurately. For example, from the existing theoretical studies for the situation of a viscous ferrofluid drop surrounded by an outer nonmagnetic fluid (i.e., single interface problem with two fluids) subjected to a radial magnetic field, the most typical morphological aspect of the resulting patterns is the formation of starlike fingered structures presenting sharp fingers [35–37]. However, by scrutinizing the linear patterns portrayed in Fig. 3, we see the formation of n-fold structures revealing the emergence of fingers that are notably rounded at their tips. The absence of sharp fingers in the ferrofluid annular structures in Fig. 3 indicate that, even though linear theory is capable of correctly predicting some of the essential effects related to the coupling of the leading and trailing interfaces, it is not able to accurately reproduce the ultimate shape acquired by the magnetically deformed ferrofluid annulus. For these reasons, in Sec. III B, we take into account the second-order perturbative terms and utilize Eqs. (13) and (14) to try to obtain a more accurate description of the interfaces' coupling and their resulting morphologies for our ferrofluid ring system at the onset of nonlinearities.

B. Nonlinear ferrofluid annulus morphologies

In this section, we turn our attention to the whole mode-coupling equations (13) and (14), taking into account the contributions coming from the intricate second-order terms [Eqs. (A1)–(A16)]. We focus on investigating the morphology of the magnetically induced annular ferrofluid structures and analyze how they are impacted by the combined action of magnetic and surface tension effects. An important aspect to be examined is to check how the controlling dimensionless parameters R, N_B, and χ influence the nonlinear dynamics of leading and trailing interfaces and the ultimate shapes of the emerging annular patterns.

We initiate our discussion by examining Fig. 4 which displays the time evolutions of a typical set of weakly nonlinear patterns for our ferrofluid annulus system. The weakly nonlinear patterns portrayed in Fig. 4 are obtained by numerically solving the second-order mode-coupling equations (13) and (14). As we did in Fig. 3 for linear patterns, here we consider the interplay of $N = 80$ Fourier cosine modes, a fundamental mode $n = 8$, and its harmonics $2n, 3n, \ldots, Nn$. To allow a direct comparison between the linear patterns of Fig. 3 and the weakly nonlinear structures illustrated in Fig. 4, all the the physical parameters and initial conditions used in Fig. 4 are equal to the ones utilized in Fig. 3. As will be justified shortly, the only difference refers to the final times taken in Figs. 4(c), 4(f), and 4(i), as opposed to the times considered in Figs. 3(c), 3(f), and 3(i). The nonlinear patterns are depicted at the times (a) $t = 7.0 \times 10^{-3}$, (b) $t = 8.0 \times 10^{-3}$, (c) $t = 1.7 \times 10^{-2}$, (d) $t = 9.5 \times 10^{-3}$, (e) $t = 1.1 \times 10^{-2}$, (f) $t = 3.4 \times 10^{-2}$, (g) $t = 1.2 \times 10^{-2}$, (h) $t = 1.4 \times 10^{-2}$, and (i) $t = 3.4 \times 10^{-2}$. As in Fig. 3, each row of Fig. 4 corresponds to a distinct time evolution for $R = 0.75$ [Figs. 4(a)–4(c)], $R = 0.92$ [Figs. 4(d)–4(f)], and $R = 0.95$ [Figs. 4(g)–4(i)].

Figure 4 is very illuminating once it permits one to identify the impact of the nonlinear effects on the shape of the evolving patterns, already at the lowest nonlinear level. Initially, for very early times, by contrasting the first column of Fig. 3 [Figs. 3(a), 3(d) and 3(g)] with the first column of Fig. 4 [Figs. 4(a), 4(d) and 4(g)], one can hardly notice any difference between linear and weakly nonlinear patterns. This is actually expected, since at very initial time stages, nonlinear effects can be ignored. However, as time increases, things

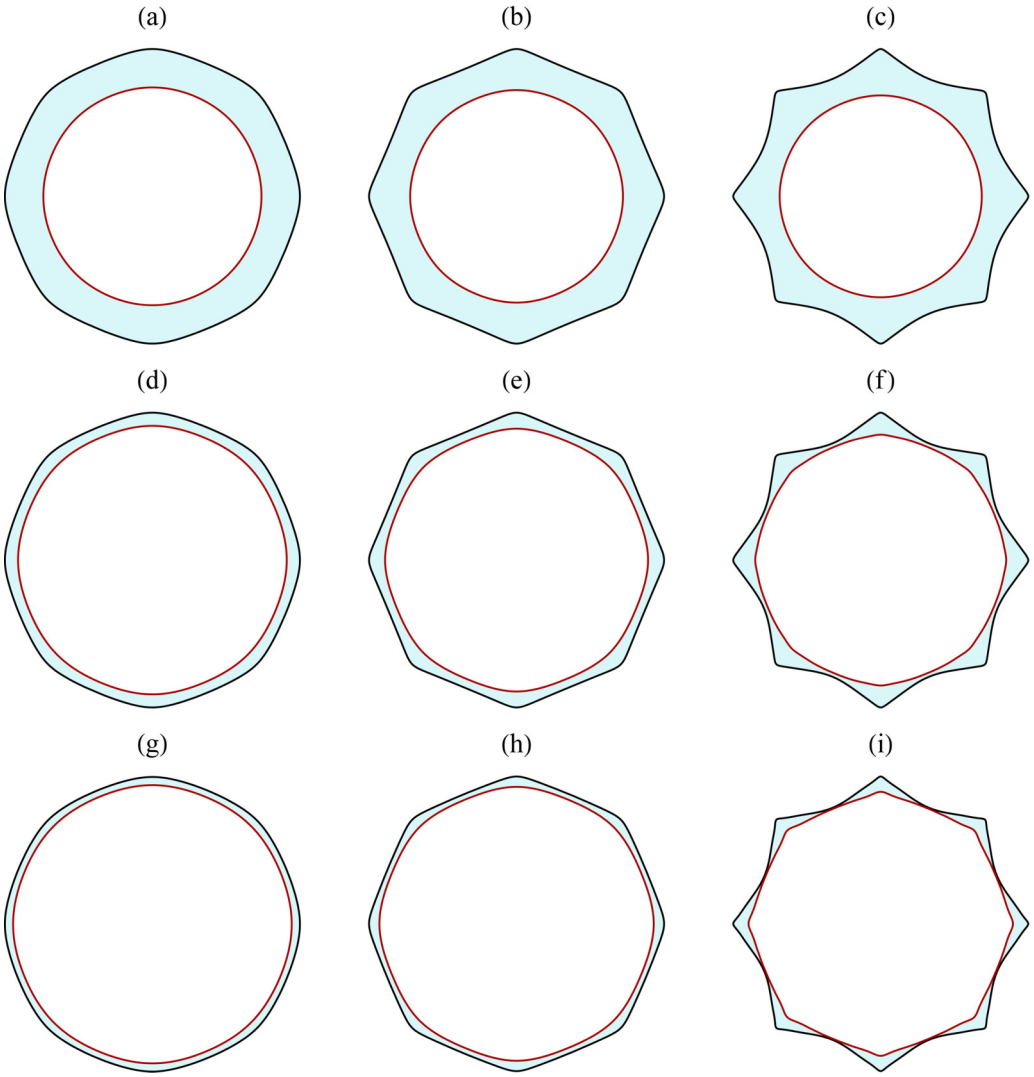

FIG. 4. Snapshots illustrating the typical weakly nonlinear evolution of the ferrofluid annulus patterns for $R = 0.75$ (top panels), $R = 0.92$ (middle panels), and $R = 0.95$ (bottom panels). Each row corresponds to a separate time evolution, and the snapshots are taken for times (a) $t = 7.0 \times 10^{-3}$, (b) $t = 8.0 \times 10^{-3}$, (c) $t = 1.7 \times 10^{-2}$, (d) $t = 9.5 \times 10^{-3}$, (e) $t = 1.1 \times 10^{-2}$, (f) $t = 3.4 \times 10^{-2}$, (g) $t = 1.2 \times 10^{-2}$, (h) $t = 1.4 \times 10^{-2}$, and (i) $t = 3.4 \times 10^{-2}$. These weakly nonlinear patterns, which have been generated by employing our second-order mode-coupling scheme, should be contrasted with the equivalent linear structures depicted in Fig. 3. All physical parameters and initial conditions used here are identical to those utilized in Fig. 3.

begin to change. This can be readily verified by comparing the second column of Fig. 3 [Figs. 3(b), 3(e) and 3(h)] with the second column of Fig. 4 [Figs. 4(b), 4(e) and 4(h)]: It is quite apparent that now the linear and weakly nonlinear patterns are different. For instance, the rounded tips and concave-shaped edges of the outer boundary of the linear shapes are replaced by outer boundaries having sharper tips and fairly straight edges in the nonlinear cases. The discrepancy between linear and weakly nonlinear morphologies is even more evident when one confronts the third column of Fig. 3 [Figs. 3(c), 3(f) and 3(i)] with the third column of Fig. 4 [Figs. 4(c), 4(f) and 4(i)]: While the linear patterns still reveal leading and trailing interfaces having blunt tips, the corresponding nonlinear annular conformations unveil their most salient differing features. Figures 4 [Figs. 4(c), 4(f) and 4(i)] reveal the formation of inner and outer nonlinear interfaces that, depending of the value of R, may present very pointy tips, assuming a characteristic starlike, n-fold polygonal shape. It is worthwhile to note that these peaky polygonal-like, annular ferrofluid morphologies for the dual-interface nonlinear situations closely resemble the typical nonlinear shapes obtained in the single interface problem of a confined ferrofluid drop under the influence of a radially applied magnetic field [35–37]. This is certainly reassuring, reinforcing the need to go beyond purely linear analysis in order to properly catch the most prominent morphological aspects of the emerging patterns in the ferrofluid annulus system.

A physical mechanism for the origin of the pointy tips that appear in the nonlinear dual-interface patterns shown in Figs. 4 [Figs. 4(c), 4(f) and 4(i)] can be given as follows. If, on the one hand, surface tension forces tend to promote the formation of rounded tips, then, on the other hand, under a radial magnetic field [Eq. (1)], the magnetic traction terms proportional to $(\hat{\mathbf{r}} \cdot \hat{\mathbf{n}})^2$ in Eqs. (11) and (12) reach their largest

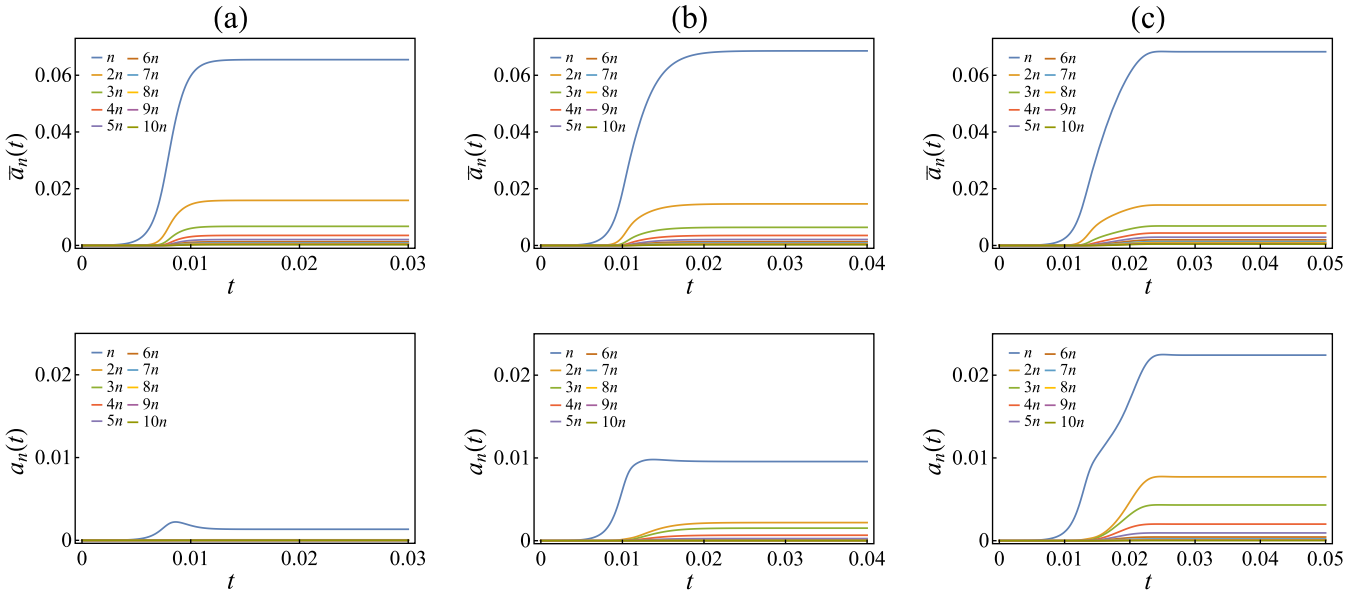

FIG. 5. Plots of the cosine amplitudes of the outer $[\bar{a}_n(t)]$ and inner $[a_n(t)]$ interfaces as a function of time t, corresponding to each time evolution presented in Fig. 4. Amplitudes for modes n, $2n$, $3n$, …, $10n$ are shown. Column (a) is related to the top row of Fig. 4. Likewise, columns (b) and (c) correspond to the middle and bottom rows of Fig. 4, respectively.

values as $\hat{\mathbf{n}}$ is collinear to $\hat{\mathbf{r}}$. In this way, once a protrusion is formed at the annular interfaces, the growing fingering structures tend to become sharper in such locations. In addition, since the applied magnetic field is proportional to the radial distance r, larger peaks arise at the leading interfaces. Moreover, from Figs. 4 [Figs. 4(c), 4(f) and 4(i)] one can see that this nonlinear peak formation mechanism becomes more effective as the parameter R is increased, due to the stronger coupling between the trailing and leading interfaces.

We continue by discussing Fig. 5 which plots the time evolution of the cosine amplitudes of the outer $[\bar{a}_n(t)]$ and inner $[a_n(t)]$ interfaces associated with the situations illustrated in Fig. 4. Although the nonlinear patterns shown in Fig. 4 are produced by considering the interplay of 80 Fourier modes, for the sake of clarity and simplicity, in Fig. 5 we only present a few representative curves. More precisely, the curves related to the time evolution of modes n, $2n$, $3n$, …, $10n$, which have sizable perturbation amplitudes. Even though the consideration of all 80 Fourier modes is important to generate accurate nonlinear shapes, having smooth peaks and edges, the curves for the perturbation amplitudes of larger Fourier modes would all overlap close to the horizontal axes, being literally indistinguishable from one another. Figure 5(a) displays how the amplitudes $\bar{a}_n(t)$ of the leading interface, and $a_n(t)$ of the trailing interface, evolve with time t, corresponding to the time-evolving patterns illustrated in Figs. 4(a)–4(c). Similarly, Figs. [5(b) and 5(c)] portrays how the perturbation amplitudes corresponding to patterns' evolutions shown in Figs. 4(d)–4(f) [Figs. 4(g)–4(i)] behave as time passes. By examining Fig. 5 one promptly identifies the most noticeable features of the curves: After an initial period of growth, all perturbation amplitudes saturate and remain unchanged as time advances. This indicates that the second-order, nonlinear ferrofluid annulus patterns tend to a stationary-state configuration. This behavior differs significantly from the equivalent linear situation of the patterns presented in Fig. 3, where the exponential growth of the perturbation amplitudes proceeds unchecked.

Now we can justify why the final times taken for the nonlinear patterns shown in Fig. 4 [Figs. 4(c), 4(f) and 4(i)] were different from the ones used in the linear patterns portrayed in Fig. 3 [Figs. 3(c), 3(f) and 3(i)]. In the linear patterns, the perturbation amplitudes grow very quickly in time, in such a way that one has to consider the largest time before interface crossing as an upper bound time for the validity of the perturbative solutions. Conversely, for the nonlinear patterns the growth of the amplitudes is attenuated, and in addition, this growth is saturated, leading to a stationary state. Therefore, while the final times taken in the linear situations Fig. 3 [Figs. 3(c), 3(f) and 3(i)] are set to avoid the crossing of the leading and trailing interfaces, the final times in the nonlinear cases Fig. 4 [Figs. 4(c), 4(f) and 4(i)] are determined by the times at which the system reaches the stationary state.

To this point, we have illustrated our main results on the behavior of the ferrofluid annulus for a representative set of parameter values, namely for $N_B = 136$, $\chi = 0.8$, $A_{12} = \mathcal{A} = 1$, $A_{23} = -1$, $R_2 = 1$, $R_1 = R$, and $\sigma = 1$. Since we were interested in understanding how the inner and outer interfaces couple together, we kept the magnetic Bond number N_B and the ferrofluid susceptibility χ constant and analyzed what happened when the interface coupling parameter R was varied. To complement our study, now we use a large but fixed value of R (to favor the coupling between inner and outer interfaces) and check how the evolving ferrofluid annulus responds to changes if N_B and χ are modified. This is done in Fig. 6, which exhibits characteristic nonlinear fluid annulus patterns by considering that $R = 0.96$, $A_{12} = \mathcal{A} = 1$, $A_{23} = -1$, $R_2 = 1$, $R_1 = R$, $\sigma = 1$, and $t = 0.1$. Our goal is to examine what happens when a couple of different values of the controlling parameters N_B ($N_B = 62$ and $N_B = 78$) and χ ($\chi = 1.3$ and $\chi = 1.7$) are used. Under these new parameter conditions the

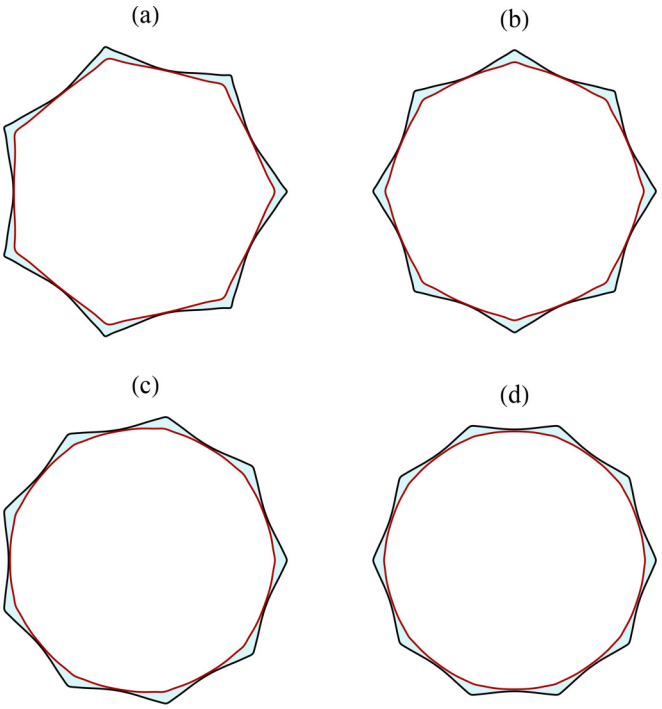

FIG. 6. Representative weakly nonlinear ferrofluid annulus patterns for (a) $N_B = 62$ and $\chi = 1.3$, (b) $N_B = 78$ and $\chi = 1.3$, (c) $N_B = 62$ and $\chi = 1.7$, and (d) $N_B = 78$ and $\chi = 1.7$. Here the patterns are plotted for $R = 0.96$, $A_{12} = \mathcal{A} = 1$, $A_{23} = -1$, $R_2 = 1$, $R_1 = R$, $\sigma = 1$, and $t = 0.1$. The number of resulting pointy fingers formed in each pattern is (a) 7, (b) 8, (c) 9, and (d) 10.

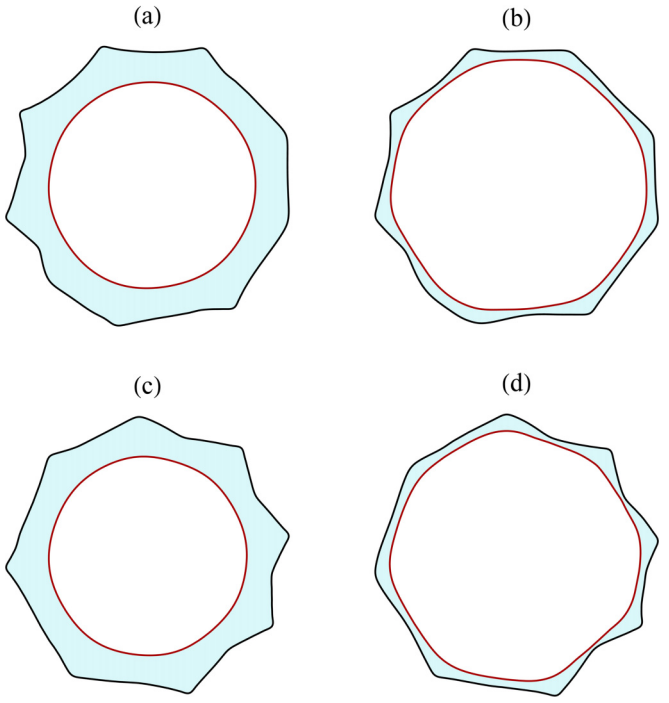

FIG. 7. Representative weakly nonlinear ferrofluid annulus patterns obtained by considering the nonlinear coupling of all sine and cosine Fourier modes in the interval $2 \leqslant n \leqslant 80$ and two different sets of random initial phases. Each row of this figure corresponds to a particular set of random initial phases, and the patterns are plotted for $R = 0.75$ and $t = 7.75 \times 10^{-3}$ [(a) and (c)] and $R = 0.92$ and $t = 9.1 \times 10^{-3}$ [(b) and (d)].

fundamental modes considered in Fig. 6 are (a) $n = 7$, (b) $n = 8$, (c) $n = 9$, and (d) $n = 10$.

In the top row of Fig. 6 the magnetic susceptibility is $\chi = 1.3$, and the magnetic Bond number assumes the values $N_B = 62$ [Fig. 6(a)], and $N_B = 78$ [Fig. 6(b)]. On the other hand, in the bottom row of Fig. 6 $\chi = 1.7$, while $N_B = 62$ [Fig. 6(c)] and $N_B = 78$ [Fig. 6(d)]. By analyzing Figs. 6(a) and 6(b) one notices the formation of typical starlike ferrofluid annular structures in which both the inner and outer interfaces are quite deformed. One can see that, keeping χ fixed and by increasing the value of N_B, the overall morphological aspects of the annular patterns are not changed dramatically, the only difference being that larger N_B results in a structure having a larger number of peaky fingers. A similar effect is also observed in Figs. 6(c) and 6(d) for a higher value of χ, also leading to the emergence of starlike-shaped ferrofluid annuli. In the end, we can see that by manipulating the values of N_B and χ one can generate peaky ferrofluid patterns presenting different number of fingers. However, the general shape of the pattern is not significantly modified. These findings support the generality of our results presented in Figs. 4 and 5.

It is worth noting that all conclusions we have reached so far regarding the basic dynamic behavior, and the most fundamental morphological aspects of the ferrofluid annuli have been illustrated by considering the formation of very symmetric n-fold structures [Figs. 3, and 4, 6]. The symmetric nature of the resulting pattern-forming shapes is due to the way the patterns have been generated, i.e., considering only cosine modes, where a fundamental mode n interacts with many of its harmonics. In addition, this has been done under a set of initial conditions in which the participating modes were only a fundamental mode n and its harmonics $2n$, $3n$, $4n$, ..., Nn, where $N = 80$. At first glance, all these circumstances may look somewhat arbitrary, but it turns out they are quite general. To make this point clear, we close this section by verifying the robustness of our main results by generating ferrofluid annulus shapes under more general circumstances. This is done in Fig. 7, where weakly nonlinear ferrofluid annulus patterns are plotted by considering a whole range of participating Fourier modes $2 \leqslant n \leqslant 80$ (note: *not* just a fundamental and its harmonics) and by assuming that all modes have the same initial amplitudes equal to 10^{-5}. To make the conditions even more general, we consider the action of both cosine and sine modes and impose two different sets of random phases attributed to each participating mode. To allow us to make a connection between the new weakly nonlinear patterns presented in Fig. 7, and the ones we portrayed in Fig. 4, the same set of relevant dimensionless parameters have been used, namely $N_B = 136$, $\chi = 0.8$, $A_{12} = \mathcal{A} = 1$, $A_{23} = -1$, $R_2 = 1$, $R_1 = R$, and $\sigma = 1$. More specifically, the weakly nonlinear ferrofluid annular patterns shown in Fig. 7 are such that for each row [i.e., in Figs. 4(a)–4(b), and in Figs. 4(c)–4(d)], we consider a distinct set of random initial phases. In this way, the patterns are plotted for $R = 0.75$ and $t = 7.75 \times 10^{-3}$ [Figs. 4(a) and 4(c)] and $R = 0.92$ and $t = 9.1 \times 10^{-3}$ [Figs. 4(b) and 4(d)].

By comparing the asymmetric patterns shown in Figs. 7(a) and 7(c) with their symmetric counterpart depicted in Fig. 4(c) one can see that, despite all differences in the way used to generate these patterns, one is still able to identify in Figs. 7(a) and 7(c) all fundamental morphological features found in Fig. 4(c). For instance, all these patterns present a relatively thick ferrofluid annulus in which the inner interface is fairly circular, while the outer interface reveals the appearance of typical peaky fingers. Likewise, by contrasting the asymmetric structures displayed in Figs. 7(b) and 7(d) with their equivalent symmetric shape illustrated in Fig. 4(f), we readily identify similarities among these patterns. For example, they all form a thin ferrofluid annulus having a less deformed trailing interface and a much more disturbed leading interface where sharp fingered tips emerge. These results reinforce the robustness of our theoretical findings and support the validity and correctness of our predictions regarding the most salient morphological aspects of confined ferrofluid annular structures induced by externally applied radial magnetic fields. Nevertheless, it should be pointed out that, in contrast to the symmetric shapes displayed in Fig. 4, the asymmetric patterns depicted in Fig. 7 do not reach a stationary state.

IV. CONCLUSION

We have considered the interfacial dynamics and pattern formation behavior of an annulus of ferrofluid, bounded by two nonmagnetic fluids, confined in a Hele-Shaw cell. Under the influence of a radial magnetic field, this magnetic fluid annular structure spreads in such a way that both the leading and trailing boundaries of the fluid ring can become unstable. One main goal of our study was to gain insight into such dual-interface unstable scenarios and try to identify and understand how the magnetic-field-induced effects impact the time evolution, and the shape of the ferrofluid annulus.

We tackled the problem theoretically and investigated both linear and weakly nonlinear stages of the dual-interface flow via a perturbative mode-coupling approach. Special attention has been given to the interactions between instabilities at the leading and trailing interfaces. Our linear stability results have shown that already at the linear regime, the inner and outer interfaces are coupled. We have found that the interaction of these two fronts is regulated by a dimensionless parameter R which measures the ratio of the outer and inner radii of the initially unperturbed annular ferrofluid layer. Lower values of R lead to the formation of thick ferrofluid annular patterns, having an undulated outer interface, and an inner one which is just mildly deformed. On the other hand, larger values of R result in the development of thin annular rings where both the inner and outer boundaries may present sizable interfacial perturbations. Moreover, our linear calculations indicate that the interfacial perturbation amplitudes grow very rapidly with time, forming n-fold ferrofluid annular patterns whose fingered structures have round tips.

All these linear findings are instructive and useful. However, the resulting linear ferrofluid annular patterns do not reveal the emergence of typical, peaky fingering shapes which commonly arise in the equivalent one-interface, two-fluid problem of a ferrofluid drop subjected to a radial magnetic field [35–37]. In order to predict and capture this important morphological feature (formation of sharp finger tips), we had to go beyond purely linear analysis. We addressed this issue by employing a second-order, weakly nonlinear analysis of the problem. By doing that, first, we have been able to confirm the correctness of the linear predictions regarding the role of the parameter R. In addition, we have also found a family of nonlinear ferrofluid annular shapes, both thin and thick, whose most remarkable morphological feature is indeed the formation of polygonal-like patterns, presenting fairly sharp fingered structures. We have verified that, depending on the value of R, these peaky fingers may arise in the outer, as well as in the inner boundaries of the ferrofluid annulus. Furthermore, we have found that nonlinear effects attenuate the growth of the perturbation amplitudes, in such a way that they eventually saturate and reach a constant value. As a result, and within the scope of our second-order theory, the symmetric, nonlinear ferrofluid annulus patterns are stationary structures.

In the weakly nonlinear regime, we have also studied the role played by two other important control parameters of the ferrofluid annulus system, namely the magnetic Bond number N_B (which expresses the relative measure between magnetic and surface tension forces) and the ferrofluids magnetic susceptibility χ, which quantifies the strength of the ferrofluid material to external magnetic stimuli. We have found that larger values of N_B and χ tend to form patterns having a larger number of sharper fingers. Finally, we also have checked that the main morphological aspects identified in our current theoretical work are fairly robust, even if different initial conditions are used or if one introduces random noise into the system.

Our present study paves the way for other explorations on the topic of interfacial instabilities and pattern formation in ferrofluid annular systems. One interesting possibility is the use of different magnetic field configurations. For instance, one could utilize the azimuthal magnetic field setup produced by a current-carrying wire oriented perpendicularly to the Hele-Shaw cell plates [32–34] or the perpendicular field arrangement generated by Helmholtz coils having electric currents flowing in the same direction [27–29]. Different applied magnetic field compositions may trigger distinct instability behaviors at the disjoint interfaces of the ferrofluid annulus. For example, for the radial magnetic field studied in this work ($H \propto r$), the outer interface is naturally more unstable than the inner boundary of the ferrofluid ring. However, if an azimuthal magnetic field ($H \propto 1/r$) is used, then we would have just the opposite scenario, making the inner interface more unstable. In this way, by using different magnetic field configurations one can magnetically induce changes in the instability of the interfaces, without having to alter the fluids' positions or their viscosities. Such a versatile magnetic tuning is obviously not available in usual versions of the three-layer Saffman-Taylor problem in a radially spreading, nonmagnetic fluid annulus [7–10]. Moreover, note that one can even exploit the utilization of more than one field configuration (e.g., by using the combined action of radial and azimuthal applied magnetic fields) in order to make both the inner and outer boundaries of the ferrofluid ring strongly unstable via purely magnetic means.

Another natural extension of this work is the development of fully nonlinear numerical simulations of the dual-interface

ferrofluid annular system, under various possible field configurations. Despite the nontrivial, doubly connected nature of the problem, such numerical simulations would open up prospects for analyzing exciting and still unexplored dynamical responses and pattern-forming structures in the long-time, fully nonlinear regime.

ACKNOWLEDGMENTS

J.A.M. thanks Conselho Nacional de Desenvolvimento Científico e Tecnológico for financial support under Grant No. 305140/2019-1.

APPENDIX: SECOND-ORDER MODE-COUPLING FUNCTIONS

This Appendix presents the expressions for the second-order mode-coupling functions which appear in the text.

In Eq. (13), the second-order terms are given by

$$F(n,n') = -\frac{\mathcal{A}|n|}{R_1}\left\{\frac{N_B}{2}\chi\{1+\chi[1+n'(n-n')]\} + \frac{\sigma}{R_1^3}\left[1-\frac{n'}{2}(3n'+n)\right]\right\}, \tag{A1}$$

$$G(n,n') = \frac{1}{R_1}\left\{A_{12}|n|[1-g_1(n,n')\,\mathrm{sgn}(nn')] - f_1^{-1}\right\}, \tag{A2}$$

$$H(n,n') = \frac{|n|}{R_2}\left\{\frac{N_B}{2}\chi\{1+\chi[1+n'(n-n')]\} - \frac{1}{R_2^3}\left[1-\frac{n'}{2}(3n'+n)\right]\right\}, \tag{A3}$$

$$I(n,n') = \frac{1}{R_2}\{A_{23}|n|[1-g_2(n')\,\mathrm{sgn}(nn')]\}, \tag{A4}$$

$$J(n,n') = \frac{|n|}{R_1}\left\{\frac{(A_{23}+1)R^{|n'|+2}}{1-R^{2|n'|}}\,\mathrm{sgn}(nn')\right\}, \tag{A5}$$

$$K(n,n') = \frac{|n|}{R_1}\left\{\frac{(A_{23}R^{2|n|}+1)R^{|n'|-|n|}}{1-R^{2|n'|}}\mathrm{sgn}(nn')\right\}, \tag{A6}$$

where

$$g_1(n,n') = \left(\frac{A_{12}+1}{2A_{12}}\right)\frac{(1+A_{23}R^{2|n|})(1+R^{2|n'|})}{(1-A_{23}R^{2|n|})(1-R^{2|n'|})} + \left(\frac{A_{12}-1}{2A_{12}}\right), \tag{A7}$$

$$g_2(n') = \frac{A_{23}+1}{A_{23}(1-R^{2|n'|})}, \tag{A8}$$

and the sgn function equals ± 1 according to the sign of its argument.

The second-order expressions in Eq. (14) are given by

$$\mathcal{F}(n,n') = H(n,n'), \tag{A9}$$

$$\mathcal{G}(n,n') = \frac{1}{R_2}\left\{A_{23}|n|[1-g_3(n,n')\,\mathrm{sgn}(nn')] - f_4^{-1}\right\}, \tag{A10}$$

$$\mathcal{H}(n,n') = F(n,n'), \tag{A11}$$

$$\mathcal{I}(n,n') = \frac{1}{R_1}\{A_{12}|n|[1-g_4(n')\,\mathrm{sgn}(nn')]\}, \tag{A12}$$

$$\mathcal{J}(n,n') = \frac{|n|}{R_2}\left\{\frac{(A_{12}-1)R^{|n'|-2}}{1-R^{2|n'|}}\,\mathrm{sgn}(nn')\right\}, \tag{A13}$$

$$\mathcal{K}(n,n') = \frac{|n|}{R_2}\left\{\frac{(A_{12}R^{2|n|}-1)R^{|n'|-|n|}}{1-R^{2|n'|}}\mathrm{sgn}(nn')\right\}, \tag{A14}$$

where

$$g_3(n') = \left(\frac{A_{23}-1}{2A_{23}}\right)\frac{(1-A_{12}R^{2|n|})(1+R^{2|n'|})}{(1+A_{12}R^{2|n|})(1-R^{2|n'|})} + \left(\frac{A_{23}+1}{2A_{23}}\right), \tag{A15}$$

and

$$g_4(n') = \frac{A_{12}-1}{A_{12}(1-R^{2|n'|})}. \tag{A16}$$

[1] For review papers see, for example, G. M. Homsy, Viscous fingering in porous media, Annu. Rev. Fluid Mech. **19**, 271 (1987); K. V. McCloud and J. V. Maher, Experimental perturbations to Saffman-Taylor flow, Phys. Rep. **260**, 139 (1995); J. Casademunt, Viscous fingering as a paradigm of interfacial pattern formation: Recent results and new challenges, Chaos **14**, 809 (2004).

[2] L. Paterson, Radial fingering in a Hele-Shaw cell, J. Fluid Mech. **113**, 513 (1981).

[3] J. D. Chen, Radial viscous fingering patterns in Hele-Shaw cells, Exp. Fluids **5**, 363 (1987).

[4] J. D. Chen, Growth of radial viscous fingers in a Hele-Shaw cell, J. Fluid Mech. **201**, 223 (1989).

[5] J. A. Miranda and M. Widom, Radial fingering in a Hele-Shaw cell: A weakly nonlinear analysis, Physica D **120**, 315 (1998).

[6] P. G. Saffman and G. I. Taylor, The penetration of a fluid into a porous medium or Hele-Shaw cell containing a more viscous liquid, Proc. R. Soc. Lond. A **245**, 312 (1958).

[7] S. S. S. Cardoso and A. W. Woods, The formation of drops through viscous instability, J. Fluid Mech. **289**, 351 (1995).

[8] T. Ward and A. White, Gas-driven displacement of a liquid in a partially filled radial Hele-Shaw cell, Phys. Rev. E **83**, 046316 (2011).

[9] P. H. A. Anjos and S. Li, Weakly nonlinear analysis of the Saffman-Taylor problem in a radially spreading fluid annulus, Phys. Rev. Fluids **5**, 054002 (2020).

[10] M. Zhao, P. H. A. Anjos, J. Lowengrub, and S. Li, Pattern formation of the three-layer Saffman-Taylor problem in a radial Hele-Shaw cell, Phys. Rev. Fluids **5**, 124005 (2020).

[11] T. H. Beeson-Jones and A. W. Woods, On the selection of viscosity to suppress the Saffman-Taylor instability in a radially spreading annulus, Fluid Mech. **782**, 127 (2015).

[12] C. Gin and P. Daripa, Stability results for multi-layer radial Hele-Shaw and porous media flows, Phys. Fluids **27**, 012101 (2015).

[13] C. Gin and P. Daripa, Time-dependent injection strategies for multilayer Hele-Shaw and porous media flows, Phys. Rev. Fluids **6**, 033901 (2021).

[14] L. Carrillo, J. Soriano, and J. Ortín, Radial displacement of a fluid annulus in a rotating HeleShaw cell, Phys. Fluids **11**, 778 (1999).

[15] L. Carrillo, J. Soriano, and J. Ortín, Interfacial instabilities of a fluid annulus in a rotating HeleShaw cell, Phys. Fluids **12**, 1685 (2000).

[16] D. Crowdy, Theory of exact solutions for the evolution of a fluid annulus in a rotating Hele-Shaw cell, Q. Appl. Math. **60**, 11 (2002).

[17] D. Crowdy, On a class of geometry-driven free boundary problems, SIAM J. Appl. Math. **62**, 945 (2002).

[18] C.-Y. Chen and S.-W. Wang, Interfacial instabilities of miscible fluids in a rotating Hele-Shaw cell, Fluid Dyn. Res. **30**, 315 (2002).

[19] C.-Y. Chen and Y.-C. Liu, Fingering instabilities of a miscible fluid annulus on a rotating Hele-Shaw cell, Int. J. Dyn. Fluids **1**, 57 (2005).

[20] V. Sharma, H. Othman, Y. Nagatsu, and M. Mishra, Viscous fingering of miscible annular ring, J. Fluid Mech. **916**, A14 (2021).

[21] M. J. Shelley, F. Tian, and K. Wlodarski, Hele-Shaw flow and pattern formation in a time-dependent gap, Nonlinearity **10**, 1471 (1997).

[22] A. Lindner, D. Derks, and M. J. Shelley, Stretch flow of thin layers of Newtonian liquids: Fingering patterns and lifting forces, Phys. Fluids **17**, 072107 (2005).

[23] J. Nase, D. Derks, and A. Lindner, Dynamic evolution of fingering patterns in a lifted HeleShaw cell, Phys. Fluids **23**, 123101 (2011).

[24] H. K. Moffatt, H. Guest, and H. E. Huppert, Spreading or contraction of viscous drops between plates: Single, multiple or annular drops, J. Fluid Mech. **925**, A26 (2021).

[25] R. E. Rosensweig, *Ferrohydrodynamics* (Cambridge University Press, Cambridge, UK, 1985).

[26] E. Blums, A. Cebers, and M. M. Maiorov, *Magnetic Fluids* (de Gruyter, New York, 1997).

[27] A. Cebers and M. M. Maiorov, Magnetostatic instabilities in plane layers of magnetizable liquids, Magnetohydrodynamics (NY) **16**, 21 (1980).

[28] A. Cebers, Dynamics of magnetostatic instabilities, Magnetohydrodynamics (NY) **17**, 113 (1981).

[29] D. P. Jackson, R. E. Goldstein, and A. O. Cebers, Hydrodynamics of fingering instabilities in dipolar fluids, Phys. Rev. E **50**, 298 (1994).

[30] S. Elborai, D.-K. Kim, X. He, S.-H. Lee, S. Rhodes, and M. Zahn, Self-forming, quasi-two-dimensional, magnetic-fluid patterns with applied in-plane-rotating and dc-axial magnetic fields, J. Appl. Phys. **97**, 10Q303 (2005).

[31] J. Kent-Dobias and A. J. Bernoff, Energy-driven pattern formation in planar dipole-dipole systems in the presence of weak noise, Phys. Rev. E **91**, 032919 (2015).

[32] J. A. Miranda, Rotating Hele-Shaw cells with ferrofluids, Phys. Rev. E **62**, 2985 (2000).

[33] D. P. Jackson and J. A. Miranda, Controlling fingering instabilities in rotating ferrofluids, Phys. Rev. E **67**, 017301 (2003).

[34] E. O. Dias and J. A. Miranda, Azimuthal field instability in a confined ferrofluid, Phys. Rev. E **91**, 023020 (2015).

[35] R. M. Oliveira, J. A. Miranda, and E. S. G. Leandro, Ferrofluid patterns in a radial magnetic field: Linear stability, nonlinear dynamics, and exact solutions, Phys. Rev. E **77**, 016304 (2008).

[36] P. H. A. Anjos, S. A. Lira, and J. A. Miranda, Fingering patterns in magnetic fluids: Perturbative solutions and the stability of exact stationary shapes, Phys. Rev. Fluids **3**, 044002 (2018).

[37] R. M. Oliveira and J. A. Miranda, Fully nonlinear simulations of ferrofluid patterns in a radial magnetic field, Phys. Rev. Fluids **5**, 124003 (2020).

[38] S. W. Haan, Weakly nonlinear hydrodynamic instabilities in inertial fusion, Phys. Fluids B **3**, 2349 (1991).

[39] H. Guo, D. C. Hong, and D. A. Kurtze, Surface-Tension-Driven Nonlinear Instability in Viscous Fingers, Phys. Rev. Lett. **69**, 1520 (1992).

[40] H. Guo, D. C. Hong, and D. A. Kurtze, Dynamics of viscous fingers and threshold instability, Phys. Rev. E **51**, 4469 (1995).

[41] E. Alvarez-Lacalle, J. Casademunt, and J. Ortn, Systematic weakly nonlinear analysis of interfacial instabilities in Hele-Shaw flows, Phys. Rev. E **64**, 016302 (2001).

[42] E. Alvarez-Lacalle, E. Paun, J. Casademunt, and J. Ortn, Systematic weakly nonlinear analysis of radial viscous fingering, Phys. Rev. E **68**, 026308 (2003).

[43] L. N. Brush and R. F. Sekerka, A numerical study of two-dimensional crystal growth forms in the presence of anisotropic growth kinetics, J. Cryst. Growth **96**, 419 (1989).

[44] L. N. Brush, R. F. Sekerka, and G. B. McFadden, A numerical and analytical study of nonlinear bifurcations associated with the morphological stability of two-dimensional single crystals, J. Cryst. Growth **100**, 89 (1990).

[45] P. P. Debroy and R. F. Sekerka, Weakly nonlinear morphological instability of a cylindrical crystal growing from a pure undercooled melt, Phys. Rev. E **53**, 6244 (1996).

[46] Z. Yu and I. C. Christov, Tuning a magnetic field to generate spinning ferrofluid droplets with controllable speed via nonlinear periodic interfacial waves, Phys. Rev. E **103**, 013103 (2021).

[47] M. Igonin, Hydrodynamic instabilities of miscible and immiscible magnetic fluids in a hele-shaw cell, Ph.D. thesis, Paris Diderot University, 2004.

[48] A. J. Dickstein, S. Erramilli, R. E. Goldstein, D. P. Jackson, and S. A. Langer, Labyrinthine pattern formation in magnetic fluids, Science **261**, 1012 (1993).

[49] C. Flament, S. Lacis, J.-C. Bacri, A. Cebers, S. Neveu, and R. Perzynski, Measurements of ferrofluid surface tension in confined geometry, Phys. Rev. E **53**, 4801 (1996).

[50] C. Flament, G. Pacitto, J.-C. Bacri, I. Drikis, and A. Cebers, Viscous fingering in a magnetic fluid. I. Radial Hele-Shaw flow, Phys. Fluids **10**, 2464 (1998).

[51] G. Pacitto, C. Flament, J.-C. Bacri, and M. Widom, Rayleigh-Taylor instability with magnetic fluids: Experiment and theory, Phys. Rev. E **62**, 7941 (2000).

[52] N. J. Hillier and D. P. Jackson, Width of a ferrofluid finger: Hysteresis and a double energy minimum, Phys. Rev. E **75**, 036314 (2007).

[53] C.-Y. Chen, Y.-S. Yang, and J. A. Miranda, Miscible ferrofluid patterns in a radial magnetic field, Phys. Rev. E **80**, 016314 (2009).

[54] C.-Y. Chen, W.-L. Wu, and J. A. Miranda, Magnetically induced spreading and pattern selection in thin ferrofluid drops, Phys. Rev. E **82**, 056321 (2010).

[55] H. Li, C.-Y. Kao, and C.-Y. Wen, Labyrinthine and secondary wave instabilities of a miscible magnetic fluid drop in a Hele-Shaw cell, J. Fluid Mech. **836**, 374 (2018).